PERGAMON

International Journal of Heat and Mass Transfer 44 (2001) 659–672

International Journal of HEAT and MASS TRANSFER

www.elsevier.com/locate/ijhmt

On multiple stability of mixed-convection flows in a chemical vapor deposition reactor

Helmar van Santen [1], Chris R. Kleijn*, Harry E.A. van den Akker

Kramers Laboratorium voor Fysische Technologie, Delft University of Technology, Prins Bernhardlaan 6, 2628 BW Delft, The Netherlands

Received 1 September 1999; received in revised form 29 February 2000

Abstract

The laminar mixed convection flow and heat transfer in a Chemical Vapor Deposition reactor are studied through numerical simulation. It is found that the non-linear interaction between forced and free convection may lead to the existence of multiple stable flows. Arclength continuation techniques, implemented within the framework of the finite volume discretisation, have been applied to determine the causes for this multiplicity. It is shown that the relevant dimensionless groups are Gr/Re and $Re \times Pr$. When both these groups are sufficiently large, multiple stable flows may exist.

1. Introduction

The IC industry shows an increasing interest in the use of so-called cold-wall single-wafer chemical vapor deposition (CVD) reactors for the purpose of depositing thin films on silicon wafers [1,2]. Generally, these reactors are based on the concept of a stagnation flow, in which a cold reactive gas mixture impinges perpendicularly onto the heated wafer, on which, as a result, a thin film is deposited. In principle, the gas flow may be 'tuned' precisely in such a way that uniform deposition and efficient removal of reaction products are obtained [3–5]. For this purpose, computational fluid dynamics (CFD) has become a widely used tool in CVD reactor design [6–9].

Single-wafer CVD reactors (see Fig. 1) typically run at operating pressures of 100–10,000 Pa. The reactor walls are cooled to room temperature, whereas the susceptor is heated to temperatures of 500–1000 K. The reactive gases are diluted in a carrier gas, typically H_2, He or N_2. The gas flow is characterized by a low Reynolds number ($Re = 1$–100), whereas the Grashof number can be relatively high, i.e. up to 10^4–10^5. The resulting flow pattern is mixed-convection, as the forced convection, owing to inlet flow, and the free convection, due to temperature differences, are about equally strong. The non-linear interaction between forced and free convection may give rise to all sorts of complex flow phenomena, which highly depend on the shape of the geometry [10–13]. In the particular geometry studied in this paper (see Fig. 1), this interaction may lead to the existence of multiple stable flows, i.e., two or more stable steady flow solutions obeying unique boundary and operating conditions [14–18].

In the commercial operation of a CVD reactor, the existence of multiple stable flows is an

* Corresponding author. Tel.: +31-15-2782835; fax: +31-15-2782838.

E-mail address: crkleijn@klft.in.tudelft.nl (Ch.R. Kleijn).

[1] Present address: Philips Research Laboratories, Eindhoven, The Netherlands.

0017-9310/01/$ - see front matter
PII: S0017-9310(00)00121-6

Nomenclature

$\mathbf{A}$	general matrix
$\mathbf{b}$	vector
c_p	specific heat of gas ($m^2/s^2/K$)
$\mathbf{e}_z$	unit vector in z-direction
g	acceleration due to gravity (m/s^2)
Ga	Gay–Lussac number $(T_{wafer} - T_{wall})/T_{ref}$
Gr	Grashof number - $g\rho_{ref}^2 L^3(T_{wafer} - T_{wall})/(\mu_{ref}^2 T_{ref})$
$\mathbf{I}$	unity tensor
$\mathbf{L}$	lower LU-decomposition matrix
L	radius vertical inflow pipe (m)
$\mathbf{M}$	precondition matrix
N_r, N_z	number of grid cells in r- and z-direction
$N(\cdot)$	constraint equation in arclength continuation
n	normal
Nu	Nusselt number, defined in Eq. (40)
$\mathbf{P}$	set of non-linear differential-algebraic equations
P	pressure ($kg/m/s^2$)
p	parameter
$\mathbf{p}$	parameter vector
$\mathbf{P}_x$	Jacobian of $\mathbf{P}$
Pr	Prandtl number $\mu_{ref} c_{p,\,ref}/\lambda_{ref}$
$\mathbf{R}$	set of non-linear differential-algebraic equations
$\mathbf{R}_u$	Jacobian of $\mathbf{R}$
r	radial coordinate (m)
Ra	Rayleigh number $Gr \cdot Pr$
Re	Reynolds number $\rho_{ref} VL/\mu_{ref}$
s	parameter of solution
T	temperature (K)
t	time (s)
$\mathbf{U}$	upper LU-decomposition matrix
$\dot{\mathbf{u}}$	time derivative of $\mathbf{u}$
$\mathbf{u}$	solution vector
V	average axial gas velocity inflow pipe (m/s)
$\mathbf{v}$	velocity vector (m/s)
$\mathbf{x}$	solution vector
z	axial coordinate (m)
ϵ	threshold in ILU(ϵ)
λ	thermal conductivity ($kg\ m/s^3/K$)
μ	dynamic viscosity (kg/m/s)
$\hat{\Phi}$	non-dimensionalized value of a variable Φ
ρ	density (kg/m^3)
τ	stress tensor ($kg/m/s^2$)
$\dagger$	transposed of a vector

unwanted phenomenon, because it leads to unpredictable process performance. With the more standard CFD tools that are generally used to design CVD reactor geometries, it is difficult to determine whether a simulated flow field at certain operating conditions is unique. As yet, uniqueness of a solution cannot be proven for a general flow problem.

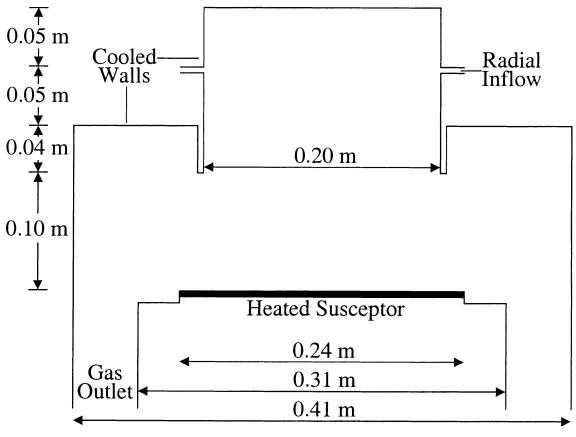

Fig. 1. Schematic of the studied cold-wall single-wafer CVD reactor.

In non-linear dynamics, however, continuation techniques have been developed that allow analysis of the phenomena such as the existence of multiple stable solutions [19]. In these methods, a path of equilibrium solutions of the flow is determined by changing one of the intrinsic parameters of the system incrementally. Yamaguchi and co-workers [20] were the first to apply these techniques in free-convection flow problems. Fotiadis and co-workers [16] were the first to exploit these techniques for studying multiple stable flows in a CVD reactor. The latter showed that the exchange of stability and the resulting existence of multiple stable flows in CVD reactors is caused by turning or limit point instabilities, and they discussed the effect of the different operating parameters on these instabilities. Both authors used the framework of a finite element method.

In this paper, the non-linear terms that actually cause these types of instabilities in single-wafer CVD reactors are isolated. This allows for the determination of the combinations of dimensionless groups that are characteristic of this phenomenon. Opposed to [16,20], the framework of the finite volume (FV) method is used in the present work. Therefore, several aspects of

the implementation of continuation and arclength techniques within this framework are discussed.

The geometry studied is an axi-symmetric vertical stagnation flow CVD reactor (see Fig. 1). The cold gases are introduced radially into a large, vertical injection tube, which is positioned perpendicularly above the horizontal susceptor surface, and leave the reactor through the annular outlet. The walls of the reactor chamber are kept at room temperature.

2. Model equations

The focus of this paper is on the mixed-convection gas flow and heat transfer in the reactor. Chemistry and species diffusion phenomena are not taken into account. When the reactants are present in high concentrations and have a molar mass that is very different from that of the carrier gas, concentration differences may lead to solutal convection [12]. Thus, the present analysis is limited to relatively dilute gas mixtures or mixtures of gases with similar molar mass. The gas flow and heat transfer in the reactor are described by the equations of mass, momentum and energy conservation. The flow is assumed to be axi-symmetric. Full 3D simulations [21] proved that this is a valid assumption for the operating conditions studied in this paper. The operating fluid is assumed to behave as an ideal gas.

Within the above constraints, the non-dimensional equations for mass, momentum, and energy conservation describing the flow in the reactor read [22]

Continuity:
$$\frac{\partial \hat{\rho}}{\partial \hat{t}} + \hat{\nabla}\cdot\left(\hat{\rho}\hat{\mathbf{v}}\right) = 0 \tag{1}$$

Momentum:
$$\begin{aligned}\frac{\partial\left(\hat{\rho}\hat{\mathbf{v}}\right)}{\partial \hat{t}} &+ \hat{\nabla}\cdot\left(\hat{\rho}\hat{\mathbf{v}}\hat{\mathbf{v}}\right)\\ &= \frac{1}{Re}\hat{\nabla}\cdot\left(\hat{\mu}\left(\hat{\nabla}\hat{\mathbf{v}} + \left(\hat{\nabla}\hat{\mathbf{v}}\right)^{\dagger}\right) - \frac{2}{3}\hat{\mu}\left(\hat{\nabla}\cdot\hat{\mathbf{v}}\right)\cdot\mathbf{I}\right)\\ &\quad - \hat{\nabla}\hat{P} - \frac{Gr}{Re^2}\left(\frac{\hat{T}-\frac{1}{2}}{\left(\hat{T}-\frac{1}{2}\right)Ga+1}\right)\mathbf{e}_z\end{aligned} \tag{2}$$

Energy:
$$\hat{c}_{\mathrm{p}}\frac{\partial\hat{\rho}\hat{T}}{\partial\hat{t}} + \hat{c}_{\mathrm{p}}\hat{\nabla}\cdot\left(\hat{\rho}\hat{\mathbf{v}}\hat{T}\right) = \frac{1}{Re\,Pr}\hat{\nabla}\cdot\left(\hat{\lambda}\hat{\nabla}\hat{T}\right) \tag{3}$$

with the following boundary conditions:

reactor walls:
$$\hat{\mathbf{v}} = 0;\quad \hat{T} = 0 \tag{4}$$

susceptor surface:
$$\hat{\mathbf{v}} = 0;\quad \hat{T} = 1 \tag{5}$$

inflow:
$$\hat{\mathbf{v}} = \hat{\mathbf{v}}_{in};\quad \hat{T} = 0 \tag{6}$$

outflow:
$$\hat{P} + \frac{\partial\hat{\tau}_{nn}}{\partial n} = 0;\quad \frac{\partial\hat{T}}{\partial n} = 0 \tag{7}$$

The different quantities have been made dimensionless as:

$$\hat{\mathbf{v}} = \mathbf{v}/V \qquad \hat{\rho} = \rho/\rho_{\mathrm{ref}} \tag{8}$$

$$\hat{T} = (T - T_{\mathrm{wall}})/(T_{\mathrm{wafer}} - T_{\mathrm{wall}}) \qquad \hat{\mu} = \mu/\mu_{\mathrm{ref}} \tag{9}$$

$$\hat{p} = (p - \rho_{\mathrm{ref}} g z))/\left(\rho_{\mathrm{ref}} V^2\right) \qquad \hat{\lambda} = \lambda/\lambda_{\mathrm{ref}} \tag{10}$$

$$\hat{\nabla} = L\nabla/V \qquad \hat{c}_{\mathrm{p}} = c_{\mathrm{p}}/c_{\mathrm{p,\,ref}} \tag{11}$$

$$\hat{t} = tL/V \tag{12}$$

where ρ_{ref}, μ_{ref}, λ_{ref} and $c_{\mathrm{p,\,ref}}$ are the values of ρ, μ, λ and c_{p} at the average gas temperature $T_{\mathrm{ref}} = \frac{1}{2}(T_{\mathrm{wafer}} + T_{\mathrm{wall}})$, L is the characteristic dimension, selected as the radius of the vertical inflow pipe, and V is the characteristic velocity, selected as the average axial gas velocity in this pipe.

The temperature dependence of the dimensionless gas properties has been fitted as:

Density:
$$\hat{\rho} = \left(\left(\hat{T}-\tfrac{1}{2}\right)Ga+1\right)^{-1} \tag{13}$$

Thermal conductivity:
$$\hat{\lambda} = \left(\left(\hat{T}-\tfrac{1}{2}\right)Ga+1\right)^{0.8} \tag{14}$$

Dynamic viscosity:
$$\hat{\mu} = \left(\left(\hat{T}-\tfrac{1}{2}\right)Ga+1\right)^{0.7} \tag{15}$$

Specific heat:
$$\hat{c}_{\mathrm{p}} = \left(\left(\hat{T}-\tfrac{1}{2}\right)Ga+1\right)^{0.1} \tag{16}$$

which is a good approximation for most common gases [23].

The set of equations (1)–(3), with material properties given by Eqs. (13)–(16), and boundary conditions (4)–(7) constitute a complete set of equations for the gas flow in the reactor as a function of the dimensionless numbers Re, Gr, Ga and Pr. The Prandtl number for gases being ~0.7, and the Gay–Lussac number varying only slightly between 0.6 and 1.0 for practical operat-

ing conditions, there are essentially two free parameters determining the gas flow: the Reynolds number via the inlet flow, and the Grashof number (and hence, the Rayleigh number) via the type of gas and operating pressure.

3. Numerical method

3.1. Discretization and solution of the flow equations

For their numerical solution, the above set of coupled non-linear partial differential equations with boundary conditions is discretized by means of a finite volume space discretization. In order to avoid problems with the odd–even decoupling of the pressures, a staggered grid is used. The convective fluxes are approximated by the second-order accurate central scheme.

The discretized equations, along with the boundary conditions, constitute a set of nonlinear differential-algebraic equations of the form:

$$\mathbf{R}(\mathbf{u}, \dot{\mathbf{u}}, \mathbf{p}) = \mathbf{0}, \tag{17}$$

where $\mathbf{u}$ is the vector of the solution, containing the velocities, temperatures and pressures in each node, $\dot{\mathbf{u}}$ the vector containing the time derivatives, and $\mathbf{p}$ is the vector of the system parameters such as *Re* and *Ra*. The steady-state solution is the solution of the system:

$$\mathbf{R}(\mathbf{u}, \mathbf{0}, \mathbf{p}) = \mathbf{0}. \tag{18}$$

where all time derivatives have been set to zero.

Usually, the system of equations (18) is solved either by use of time integration [24] or by use of relaxation methods [25]. In these methods, the momentum and energy equations are decoupled from the continuity equations using pressure-correction schemes. Advantage of these methods is that the resulting sets of linear equations have favorable spectral properties. Therefore, they can be solved efficiently. A disadvantage is that a relatively large number of time steps or iterations are required. This, however, can partly be overcome by use of multi-grid acceleration [26,27].

A more important disadvantage, however, is that only a subset of the solutions of Eq. (18) can be computed, since these methods only converge to linearly stable solutions. In the study of flow instabilities and transitions such as multiple stable flows, the capability to calculate all (stable and unstable) solutions is essential. Most solution methods that are capable of calculating all solutions of a set of non-linear equations are based upon Newton's method [28]. It converges to any solution of the discretized flow equations, stable or unstable, provided that the initial estimate is sufficiently close to this solution. For the FV discretized incompressible flow equations, these methods are rarely used [29]. Relaxation and time-stepping methods are generally preferred, because they can be more easily implemented, and because their demands on computing time and memory are generally lower.

Newton's method for solving Eq. (18) can be written as:

$$\mathbf{R}_u\left(\mathbf{u}^{(n)}, \mathbf{0}, \mathbf{p}\right)\left[\mathbf{u}^{(n+1)} - \mathbf{u}^{(n)}\right] = -\mathbf{R}\left(\mathbf{u}^{(n)}, \mathbf{0}, \mathbf{p}\right) \tag{19}$$

where $\mathbf{R}_u$ is the global Jacobian of the system of equations $\mathbf{R}$:

$$\mathbf{R}_u = \frac{\partial \mathbf{R}}{\partial \mathbf{u}} \tag{20}$$

This method converges quadratically, provided that the initial guess $\mathbf{u}^{(0)}$ is sufficiently close to the actual solution. Several methods are available to enlarge the radius of convergence [30]. In flow problems, this is not a serious restriction: for stable solutions, a few large time steps can be taken to arrive at a good initial guess. For unstable solutions, continuation techniques as discussed below are available.

The Jacobian $\mathbf{R}_u$ has been obtained analytically, as this method is computationally more efficient, and is less sensitive to numerical errors than numerical differentiation. In the momentum and energy equations, however, the derivative of the fluid properties to temperature has been taken into account in gravity terms only. This may lead to linear convergence of the Newton solver when the terms ignored become important; this is the topic of Section 3.3.

3.2. Linear solvers

In each iteration of the Newton solver, a linear system of equations has to be solved:

$$\mathbf{A}\mathbf{x} = \mathbf{b} \tag{21}$$

Where $\mathbf{A}$ is a sparse matrix with dimension four times the grid size, since there is an equation for each variable (i.e. two velocity components, temperature and pressure) in each point. The spectral properties of $\mathbf{A}$ are bad, especially as a result of the zeros at the diagonal of the discrete mass conservation equations.

In this paper, the Krylov-subspace method GMRES (Generalized Minimum RESidual) has been applied [31–34]. Krylov-methods are semi-iterative methods, as in exact arithmetic the solution vector can be found within a finite number of iterations, equal to the dimension of the system. In practice, however, these methods are only efficient if the solution can be found in a fraction of this number. The number of iterations required by GMRES to find the solution is determined by the number of basis vectors needed to meet a cer-

tain convergence criterion. A system with favorable spectral properties, usually corresponding to a diagonally dominant system, can be solved within a few iterations. The spectral properties of the system resulting from the discretized flow equation, Eq. (18), however, are bad. To overcome this problem, preconditioning is applied. Rather than the system of Eq. 21, the system:

$$\mathbf{M}^{-1}\mathbf{A}\mathbf{x} = \mathbf{M}^{-1}\mathbf{b} \tag{22}$$

is solved. Here $\mathbf{M}$ is the precondition matrix, or preconditioner, and is selected in a way that $\mathbf{M}$ resembles $\mathbf{A}$ and $\mathbf{M}\mathbf{x} = \mathbf{b}$ can be solved cheaply. Many different preconditioners have been proposed, especially for simple, comparatively well-posed systems [33–36]. A general strategy applicable to more general systems is not available.

Ideally, $\mathbf{M}$ equals $\mathbf{A}$. Then, GMRES converges in a single iteration. One option is to select $\mathbf{M}$ according to:

$$\mathbf{M} = \mathbf{L}\mathbf{U} = \mathbf{A} \tag{23}$$

This, however, is equivalent to directly solve the system which is inefficient. $\mathbf{M}$ only has to resemble $\mathbf{A}$. A good alternative therefore is to determine $\mathbf{M}$ such that:

$$\mathbf{M} = \mathbf{L}\mathbf{U} \approx \mathbf{A} \tag{24}$$

This approach has been selected in this paper. A so-called Incomplete LU (ILU) decomposition of $\mathbf{A}$ is generated by determining the normal LU decomposition of $\mathbf{A}$ with the restriction that only the elements larger than some threshold ϵ are taken into account. This decomposition is called ILU(ϵ) or ILUT.

In literature, different preconditioners have been suggested [37,38]. However, the preconditioners suggested in literature are less efficient in taking advantage of the special properties of $\mathbf{A}$ for the currently studied flows. Since the Reynolds and Grashof numbers are relatively low, the convection terms are rather small compared to the diffusion terms. The latter (and thus the coefficients in matrix $\mathbf{A}$) are therefore virtually independent of the flow. A single ILU(ϵ) decomposition then suffices for the whole Newton solver.

For the ILU(ϵ) preconditioner, the ordering of the equations is of importance. In this paper, the nodes are numbered from left to right and line-wise from below to the upper boundary. Then, for each node, all variables are grouped together:

$$\mathbf{x}^{\dagger} = \left(v_r^{1,1}, v_z^{1,1}, T^{1,1}, P^{1,1}, \ldots, v_r^{N_r,N_z}, v_z^{N_r,N_z}, T^{N_r,N_z}, P^{N_r,N_z}\right) \tag{25}$$

The advantage of this ordering method is that the complete LU decomposition is a band matrix. The fill-in of the ILU of a band matrix therefore is limited to this band reducing the chance of memory problems.

3.3. Implementation and efficiency

The above numerical method has been implemented in FORTRAN. All floats are double precision except for those in the precondition matrix, which is relatively large, and only an approximation.

An excellent check on the implementation is the convergence behaviour of the Newton solver. This solver must converge quadratically when the Gay–Lussac number is small. Small errors in the discretization, even for a single cell, may lead to linear convergence.

In Fig. 2, the convergence is depicted for $Re = 3$ and $Gr = 1000$, with $Ga = 0$ and 0.8, respectively. The grid is $N_r \times N_z = 63 \times 105$. The figure illustrates that convergence for low Ga is indeed quadratic, but that when Ga is increased, convergence becomes linear. The reason is that the quadratic Newton solver then effectively turns into a linear Picard solver. Still, very low residuals can be attained in a limited number of iterations, especially compared to time-stepping or relaxation methods. Furthermore, the most important goal for using this type of solvers, i.e. being able to compute linearly unstable flows, remains intact.

The most time-consuming step in this method is solving the linear system resulting from Eq. (19). This step consists of once generating an ILU(ϵ) and using this decomposition in each of the GMRES steps. There are several parameters that affect the efficiency,

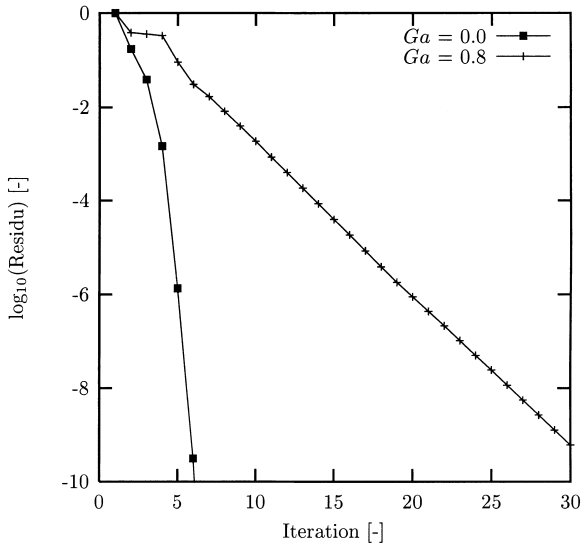

Fig. 2. Convergence of the coupled solvers ($Re = 3$, $Gr = 1000$).

viz. the threshold ϵ, the restart m in GMRES, and the convergence criterion. With the ILU(ϵ) preconditioner used, a restart is rarely necessary. GMRES then usually converges either within 50 GMRES steps or not at all. Hence, m is set to 60. For the convergence criterion, a preconditioned residual of $O(10^{-6})$ is used. This is usually sufficiently low to guarantee quadratic convergence for the Newton solver. Unfortunately, the convergence criterion can not be selected independently of the threshold chosen in the preconditioner.

In the selection of the threshold, the most important aspects are the memory required to store the ILU matrix, the computing time required for the generation, and the computing time required in the GMRES solver. In the computations presented below, ϵ is selected $O(10^{-6})$. The resulting fill-in is relatively high: for a $N_r \times N_z = 70 \times 42$ grid with $Re = 3$ and $Gr = 1000$, the fill-in is approximately 80% of the band. Then the total computation time for a single 100 MHz HP8000 processor of a Convex S-class server is 90 s, showing that the flows can be calculated comparatively efficiently. For larger grids or in three dimensions, however, demands on the memory may become too large and/or break-down may occur.

In the simulations presented below, the grid is selected $N_r \times N_z = 63 \times 105$. For a representative set of flow conditions, doubling the grid to $N_r \times N_z = 126 \times 210$ resulted in a less than 1% change in the heat flux everywhere on the susceptor surface.

4. Multiple solutions and turning-point instabilities

The multiple stable flows that may occur in the geometry studied, can be attributed to turning-point or limit-point instabilities. In order to study these instabilities, a numerical method is implemented that allows computation of the solution branch, including the turning points, as a function of one of the operating parameters. This method can be separated into two parts: (i) a continuation technique to follow a solution branch as a function of an operating parameter such as the Reynolds number; (ii) Keller's pseudo-arclength procedure to track a solution through a turning point [19]. These two steps are presented below, in a notation similar to Fotiadis [16].

4.1. Continuation in an operating parameter

For steady-state problems, Eq. (17) can be rewritten as:

$$\mathbf{R}(\mathbf{u}(\mathbf{p}), \mathbf{p}) = \mathbf{0} \tag{26}$$

Where the parameter set $\mathbf{p}$ contains the system parameters such as geometry, Re and Gr. To determine the effect of one parameter, say p, continuation techniques are used to produce the initial estimate for the next Newton iteration. To simplify the notation, rather than the parameter set $\mathbf{p}$, just one parameter, p, is selected. This is the parameter that currently changes. For steady-state problems, Eq. (26) then can be rewritten as:

$$\mathbf{R}(\mathbf{u}(p), p) = \mathbf{0} \tag{27}$$

The first-order Taylor expansion for the solution vector at a neighboring value $p + \Delta p$ is given by:

$$\mathbf{u}(p + \Delta p) = \mathbf{u}(p) + \frac{\partial \mathbf{u}(p)}{\partial p}\Delta p \tag{28}$$

The tangent vector, $\partial \mathbf{u}(p)/\partial p$, is calculated from the set of linear equations for the directional derivative of Eq. (26) along the solution family at p:

$$\mathbf{R}_u(\mathbf{u}(p), p)\frac{\partial \mathbf{u}(p)}{\partial p} = -\frac{\partial \mathbf{R}(\mathbf{u}(p), p)}{\partial p} \tag{29}$$

Since for solving Eq. (29) the same Jacobian is used as for solving Eq. (19), no new ILU(ϵ) needs to be generated. First-order continuation requires only the vector of parameter derivatives of the equations to be calculated, and the solution of system (29) is cheap since the ILU(ϵ) is available.

Solving Eq. (29) gives an initial estimate for $\mathbf{u}(p + \Delta p)$. The actual solution then can be calculated using the Newton method presented in the previous section.

4.2. Tracking through turning points

If $\mathbf{R}_u$ is non-singular, a unique solution in the neighborhood of p exists. The above method fails to converge close to turning points, since $\partial \mathbf{u}(p)/\partial p$ will grow unboundedly as p approaches the singular point. Furthermore, the initial guess $\mathbf{u}(p + \Delta p)$ may be far from the solution branch.

The arclength continuation method can be used to overcome this problem. In this method, an additional parameter, s, is introduced, the so-called independent parameter of the solution arc. This new parameter requires an additional equation and this equation is selected in such a way that the solution branch has no turning points in parameter s. Rather than tracking a solution as a function of parameter p, the parameter s is used. A positive change in s causes either a positive or a negative change in p. The sign of the change in p changes at a turning point. Computing the solution branch as a function of s therefore allows tracking of the whole solution branch, including the turning points and the unstable branch.

The additional constraint that is added to the solution is denoted with $N(\mathbf{u}, p, s)$. The problem Eq. (27)

then changes to:

$$\mathbf{R}(\mathbf{u}, p) = \mathbf{0}$$

$$N(\mathbf{u}, p, s) = 0 \tag{30}$$

where s is the independent parameter of the solution arc. $N(\mathbf{u}, p, s)$ is chosen such that s resembles the 'arclength' of the solution branch, resulting in:

$$\left(\frac{\partial \mathbf{u}}{\partial s}\right)^{\dagger}\left(\frac{\partial \mathbf{u}}{\partial s}\right) + \left(\frac{\partial p}{\partial s}\right)\left(\frac{\partial p}{\partial s}\right) = 1 \tag{31}$$

The interpretation of this equation is illustrated in Fig. 3. This figure also illustrates that with this selection for $N(\mathbf{u}, p, s)$, no singularities can be expected in s at a turning point.

The continuation technique as presented in the previous section is applied to the extended system of equations, Eq. (30), which is defined as:

$$\mathbf{P}(\mathbf{x}, s) = \begin{bmatrix} \mathbf{R}(\mathbf{u}, p) \\ N(\mathbf{u}, p, s) \end{bmatrix} = \mathbf{0} \tag{32}$$

where $\mathbf{x}$ is the solution vector ($\mathbf{x} = [\mathbf{u}(s), p(s)]^{\dagger}$).

Suppose that at s the solution is $\mathbf{x} = [\mathbf{u}(s), p(s)]^{\dagger}$. Similar to Eq. (28), a good initial guess for the solution at $s = s + \Delta s$ then can be determined from:

$$\mathbf{u}(s + \Delta s) = \mathbf{u}(s) + \Delta s \frac{\partial \mathbf{u}(s)}{\partial s}$$

$$p(s + \Delta s) = p(s) + \Delta s \frac{\partial p(s)}{\partial s} \tag{33}$$

Because $\mathbf{R}(\mathbf{u}(s), p(s)) = \mathbf{0}$ holds at s, we have

$$\left(\|\frac{\partial \mathbf{u}(s)}{\partial s}\|_2\right)^2 + \left(\frac{\partial p(s)}{\partial s}\right)^2 = 1 \tag{34}$$

where $\|u\|_2$ is the L_2-norm of $\mathbf{u}$. Now, from Eq. (34), and using the chain rule, expressions can be derived for the partial derivatives $\partial \mathbf{u}(s)/\partial s$ and $\partial p(s)/\partial s$ in Eq. (33):

$$\frac{\partial p(s)}{\partial s} = \pm\left(1 + \|\frac{\partial \mathbf{u}(s)}{\partial p}\|_2^2\right)^{-\frac{1}{2}} \tag{35}$$

and

$$\frac{\partial \mathbf{u}(s)}{\partial s} = \left(\frac{\partial \mathbf{u}(s)}{\partial p}\right)\left(\frac{\partial p(s)}{\partial s}\right) \tag{36}$$

The sign of Eq. (35) is such that:

$$\left(\frac{\partial \mathbf{u}(s)}{\partial s}\right)^{\dagger}\big(\mathbf{u}(s) - \mathbf{u}(s - \Delta s)\big) + \frac{\partial p}{\partial s}\big(p(s) - p(s - \Delta s)\big) > 0 \tag{37}$$

while $\partial \mathbf{u}(s)/\partial p$ in Eqs. (35) and (36) is obtained by solving the linear system (29).

With the initial guess from Eq. (33), Newton's method is applied to Eq. (32) where the arclength condition, Eq. (34) is linearized:

$$N(\mathbf{u}, p, s) = \left(\frac{\partial \mathbf{u}(s)}{\partial s}\right)^{\dagger}\big(\mathbf{u}(s) - \mathbf{u}(s + \Delta s)\big) + \frac{\partial p}{\partial s}\big(p(s) - p(s + \Delta s)\big) - \Delta s = 0 \tag{38}$$

There is one important difference between tracking in s and tracking in p. In contrast to the Jacobian $\mathbf{R}_u$, the Jacobian of $\mathbf{P}(\mathbf{x}(s), s)$, given by:

$$\mathbf{P}_x(\mathbf{x}(s), s) = \begin{bmatrix} \mathbf{R}_u & \dfrac{\partial \mathbf{R}}{\partial p} \\ \dfrac{\partial N}{\partial \mathbf{u}} & \dfrac{\partial N}{\partial p} \end{bmatrix} \tag{39}$$

remains non-singular on the solution branch, thus also at turning points in p [19]. This property allows tracking of the whole solution branch.

The numerical method presented above has been implemented using the Reynolds number for the parameter p.

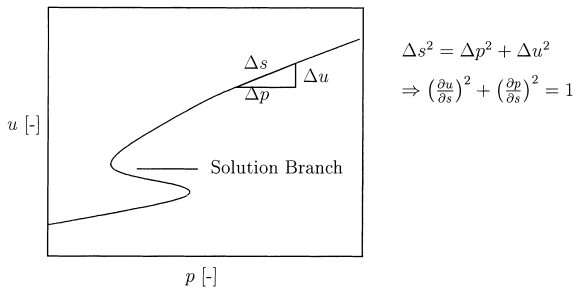

Fig. 3. Selection of the equation for s.

5. Results and discussion

5.1. Introduction

We have studied mixed-convection flows in the reactor depicted schematically in Fig. 1. The walls are cooled to a uniform temperature T_{wall}, the wafer is

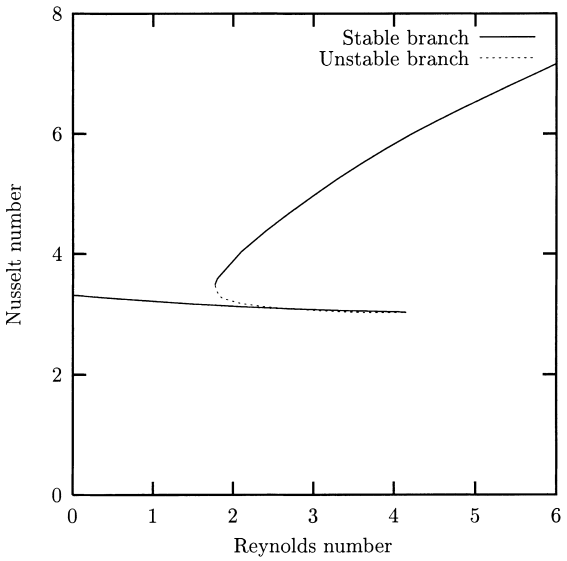

Fig. 4. Bifurcation diagram at $Gr = 1000$, $Ga = 0.8$ and $Pr = 0.7$.

heated to a uniform temperature T_{wafer}. In actual reactor operation, small non-uniformities in wall temperatures cannot be avoided. These are not, however, expected to significantly influence the overall flow pattern. The influence of various operating conditions (type of carrier gas, pressure, flowrate and wafer temperature, see Introduction) on the mixed convection flow is studied through a variation of the characteristic dimensionless numbers, i.e. *Re*, *Gr* and *Ga*.

It has been shown earlier, that multiple stable flows in the geometry under study exist for $Re = 3$, $Gr = 1000$, $Ga = 0.8$, and $Pr = 0.7$ [18]. These are realistic operating conditions in CVD processes, e.g. for N_2 as the carrier gas corresponding to an operating pressure of 1.3 kPa, an inlet flow-rate of 3.7×10^{-5} kg/s,[2] a wall temperature of 300 K, and a wafer temperature of 700 K. Here, we use the numerical method presented above to determine the characteristics of the different solutions at these conditions, and to show that the observed multiplicity can be attributed to turning-point instabilities.

In Fig. 4 the computed bifurcation diagram has been plotted as function of the Reynolds number. As a measure of the solution, the average Nusselt number across the wafer surface is chosen:

$$Nu = \frac{1}{\pi \hat{r}_{\text{wafer}}^2} \sum_{i=0}^{N_{r,\text{ wafer}}} \pi \left(\hat{r}_{i+\frac{1}{2}}^2 - \hat{r}_{i-\frac{1}{2}}^2 \right) \hat{\lambda}_i \left(\frac{\partial \hat{T}}{\partial \hat{z}} \right)_i \tag{40}$$

[2] Corresponding to 1.85 slm (standard liters per minute).

Fig. 5 shows the three solutions that exist at $Re = 3$. For these three solutions, Fig. 6 presents the local Nusselt numbers as a function of the radial coordinate.

Fig. 4 shows that the multiple stable flows in this geometry are the result of two turning-point instabilities: one at $Re = 4.15$, and one at $Re = 1.77$. These can be readily computed with the numerical method presented above, provided that the step size Δs is selected small near the turning points in order to remain on the solution branch.

For low inlet Reynolds numbers, the flow in the reactor is dominated by free convection. This produces a large buoyancy-induced recirculation cell, filling up almost the whole reactor (see Fig. 5(A)). Increasing the inlet Reynolds number from 0 to 4.15 only slightly changes the average Nusselt number. This part of the solution branch is called the lower stable solution branch.

At $Re = 4.15$, the lower turning point is found and the unstable solution branch begins. This means that, if time-stepping with a sufficiently small time step were performed from an initial guess at this unstable branch, the solution would diverge from this branch to one of the stable branches. Compared to the lower, stable branch, the recirculation at the unstable branch becomes smaller and is pushed away from the wafer (see Fig. 5(B)). In this region, a reduction of the inlet Reynolds number has little effect on the average heat transfer.

The upper stable solution branch starts at $Re = 1.77$. On this branch, the forced convection dominates the flow above the wafer and the buoyancy-induced recirculation is pushed further away from the wafer (see Fig. 5(C)). This causes an increase in the heat transfer near the center of the wafer (see Fig. 6). When the Reynolds number is further increased, the recirculation disappears completely.

The range of Reynolds numbers between 1.77 and 4.15 is called the multiplicity region, since three solutions, two stable and one unstable, exist. In practical reactor operation, small coincidences in the startup of the reactor may determine which of the two stable steady flows is settled. For all operating conditions with a multiplicity region as discussed further in this paper, the main characteristics of flow and heat transfer on the three branches are similar to those plotted in Fig. 5.

In the next section, the non-linear terms in the flow equations that cause this phenomenon, are isolated.

5.2. Sources of multiplicity

Multiple stable flows are due to non-linear effects. In the flow equations, the non-linear terms that may be the source of such an effect therefore are: (i) the

convection terms in the momentum equations, Eq. (2); (ii) the convection terms in the energy equation, Eq. (3); (iii) the non-linear gravity term in the momentum equations, Eq. (2); (iv) the dependency of density on temperature in the mass conservation equation, Eq. (1); (v) the dependency of further material properties on temperature. Contributions (iii)–(v) are linear in the Boussinesq approximation, here corresponding to the limit of $Ga \rightarrow 0$. At conditions where this limit holds, however, a multiplicity region is still found, although

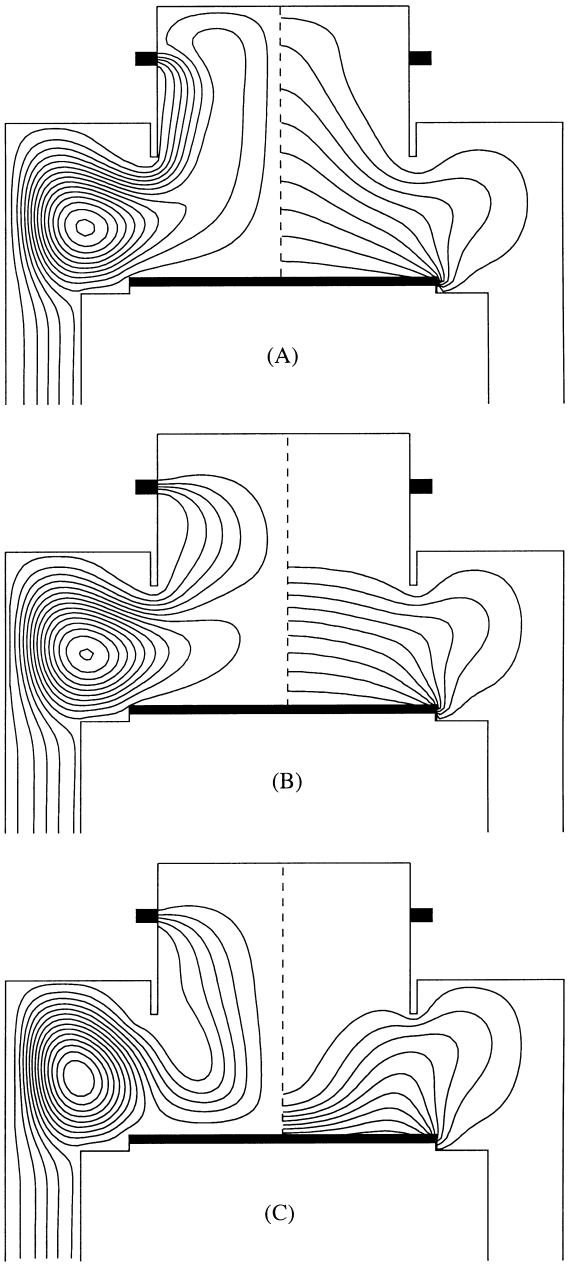

Fig. 5. Three solutions at $Re = 3$, $Gr = 1000$, $Ga = 0.8$ and $Pr = 0.7$: (A) stable free-convection dominated solution, (B) unstable solution, and (C) stable forced-convection dominated solution. The left side shows the dimensionless streamlines with intervals of 0.2, the right-hand side the dimensionless temperature from 0.1 (closest to the cold walls) to 0.9 (closest to the wafer surface), with intervals of 0.1.

at slightly higher Grashof number. The non-linearities (iii)–(v), therefore, are not essential for the existence of multiple stable flows.

The effect of the convection terms in the momentum equations (source (i)) is negligible at low Reynolds numbers. In the Boussinesq approximation, the momentum and energy equations then reduce to:

$$\hat{\nabla}^2\hat{\mathbf{v}} + \hat{\nabla}(Re\,\hat{p}) + \frac{Gr}{Re}\left(\hat{T} - \frac{1}{2}\right)\mathbf{e}_z = 0 \tag{41}$$

$$Re\,Pr\hat{\nabla}\cdot(\hat{\mathbf{v}}\hat{T}) - \hat{\nabla}^2\hat{T} = 0 \tag{42}$$

Eqs. (41) and (42) show that at these low Reynolds numbers, the dimensionless parameters uniquely defining the flow are Gr/Re and $Re \times Pr$.

To study this limit, the solution branch has been computed for two different cases: in the first case, $Re = O(1)$, $Gr = 1000$ and $Pr = 0.7$. In the second case, the Reynolds and Grashof numbers are scaled down by a factor 1000 to $Re = O(10^{-3})$ and $Gr = 1$, whereas Prandtl is increased by that same factor to $Pr = 700$, thus keeping Gr/Re and $Re \times Pr$ constant. In Fig. 7, the two resulting solution branches have been compared. This figure shows that a drastic decrease of Re causes only limited quantitative differences. Apparently, the scaling of Eqs. (41) and (42), based on the assumption that the convection terms in the momentum equations are comparatively small, even holds at Reynolds numbers as large as $Re \sim 3$. More importantly, however, this figure shows that multiplicities still occur at Reynolds numbers as low as $Re = O(10^{-3})$, proving that the convection terms in the momentum equations are not the cause of the existence of multiple stable flows. The only remaining non-linear term, and thus the cause of this phenomenon, is the convection term in the energy conservation equation (source (ii)).

For a given geometry, the two important parameters therefore are:

- Gr/Re, which can be interpreted as the strength of momentum transport owing to buoyancy, compared to molecular transport of momentum;
- $Re \times Pr$, which is the ratio of convective and diffusive transport of energy.

These determine whether or not the solution is in a multiplicity region. The effect of these two parameters has been plotted in Fig. 8.

Fig. 8 shows that when the buoyancy is sufficiently strong compared to molecular transport of momentum, and, when the convective transport of energy is sufficiently high compared to the diffusive transport of energy, a flow solution is in a multiplicity region. In this geometry, the minimum is approximately at $Gr/Re = 200$ and $Re \times Pr = 1.5$.

For ideal gases in incompressible flows, where the Boussinesq approximation does not hold, the convection terms in the energy equation are linear, as the product of ρ and $\hat{T}$ then is a constant. In that case it is impossible that they cause multiple stable flows. Then, however, a similar term appears in the mass conservation equations: $\mathbf{v}\cdot\nabla T$ in turn becoming the source of

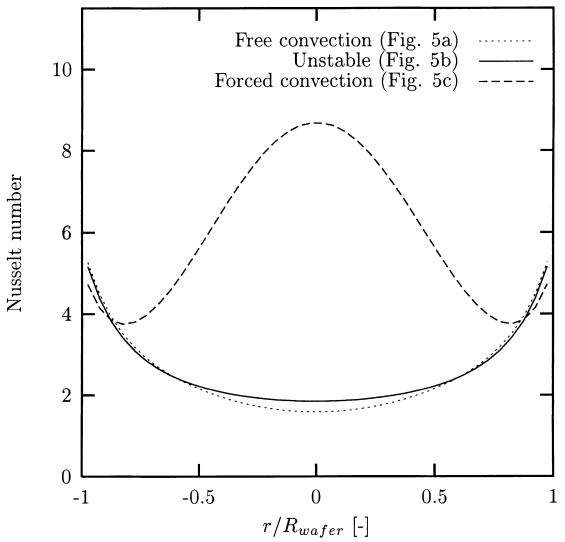

Fig. 6. Heat flux of the three solutions at $Re = 3$, $Gr = 1000$, $Ga = 0.8$ and $Pr = 0.7$.

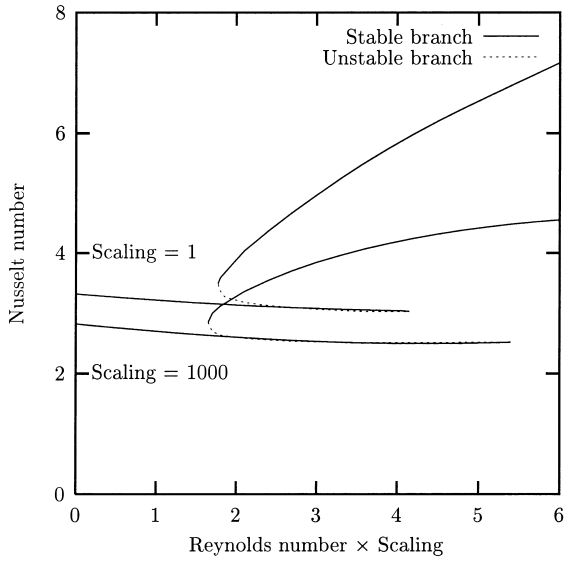

Fig. 7. Effect of scaling down the Reynolds number by a factor 1000, keeping Gr/Re and $Re \times Pr$ constant at $Ga = 0.8$.

the non-linearity. For ideal gases, therefore, $Re \times Pr$ and Gr/Re remain the two important parameters.

Above, the terms in the flow equations that may cause a multiplicity region have been isolated for $Ga \to 0$ and variable Prandtl number. The Prandtl number of most common gases, however, is constant and about 0.7, whereas in CVD reactors $Ga \sim 0.6$–1. Therefore, below, the multiplicity phenomena in this reactor are studied by varying Gr and Ga as a function of Re.

5.3. The influence of the Grashof number

For a fixed geometry and a fixed gas, the Grashof number is mainly determined by the operating pressure. In practice, a large range of Grashof numbers can be obtained with relatively small pressure variations, because Gr increases with the square of the operating pressure. As an example, with nitrogen as the carrier gas, operating pressure of 130 and 1300 Pa correspond to Grashof numbers of 10 and 1000, respectively. The Grashof number is linearly contained in the gravity term, one of the important terms for multiple solution phenomena. Increasing Gr therefore can be expected to increase the multiplicity region.

Fig. 9 shows the effect of Gr for $Ga = 0.8$ and $Pr = 0.7$. The solution branches at $Gr = 500$, 1000, 1500 and 2000 are shown. $Gr = 500$ corresponds to the point just outside the multiplicity region. As expected, increasing Gr leads to increasing the range of Reynolds numbers where there is more than one stable flow.

5.4. The influence of the Gay–Lussac number

The Gay–Lussac number, $2(T_{\text{wafer}} - T_{\text{wall}})/(T_{\text{wall}} + T_{\text{wafer}})$ is bounded between 0 and 2. $Ga = 0$ corresponds to the Boussinesq approximation and $Ga = 2$ corresponds to a high wafer temperature compared to the wall temperature. In practice, Gay–Lussac numbers up to ~ 1 ($T_{\text{wall}} = 300$ K and $T_{\text{wafer}} = 900$ K) can be expected.

Provided that the effect of Ga on μ, c_p, λ and the convection term in the momentum equation are ignored, the driving temperature difference is still important at two points in the flow equations, viz. the factor $Ga \times \{[\hat{T} - (1/2)]Ga + 1\}^{-1}$ in the non-linear term in the mass conservation equation (see Eq. (1)) and $((\hat{T} - 1/2)Ga + 1)^{-1}$ in the gravity term in the momentum equations, Eq. (2). These factors are non-linear and can become large in low temperature areas when Ga is large. It can thus be expected that the multiplicity region increases super-linearly with Ga.

In Fig. 10, the effect of Ga is shown for $Gr = 1000$ and $Pr = 0.7$. The solution branches at $Ga = 0.1$, 0.5, 0.8 and 1 are shown. As expected, the multiplicity region increases with increasing Ga. Furthermore, the Nusselt number slightly increases with Ga, as the transport coefficients such as λ at the wafer surface increase.

6. Concluding remarks

In the cold wall single-wafer CVD reactor studied, multiple stable flows may occur as a result of turning-point instabilities.

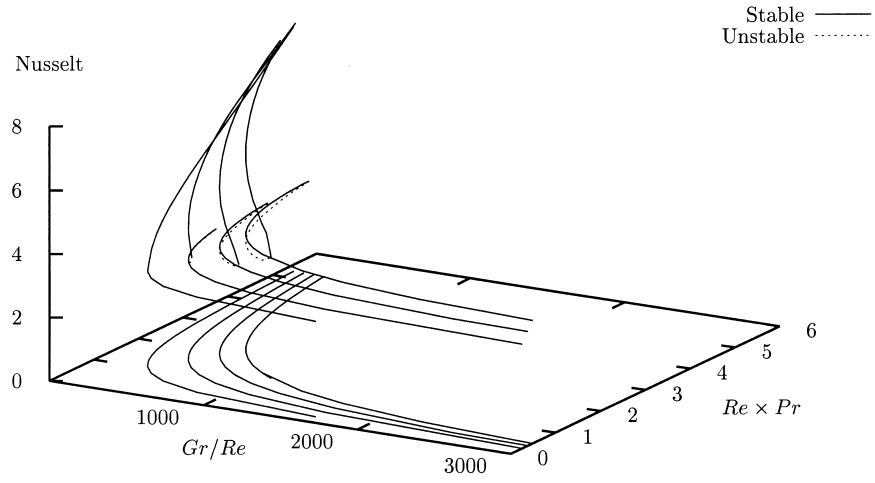

Fig. 8. Solution branches as a function of the main parameters Gr/Re and $Re \times Pr$ at $Ga = 0.8$.

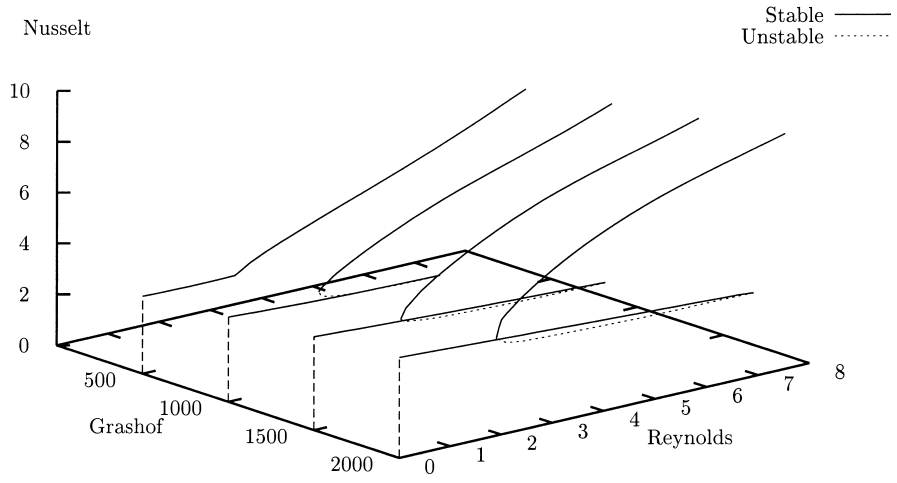

Fig. 9. Effect of Gr on the multiplicity region at $Ga = 0.8$ and $Pr = 0.7$.

An arclength continuation technique in combination with a Newton/Picard solver has been implemented within the framework of a FV method. This allows efficient tracking of the solution branches through these turning-point instabilities. The most time- and memory-consuming step is the linear solver in the Newton iterations. GMRES in combination with an ILU(ϵ) preconditioner performs well for these low Reynolds number flows. Due to the large fill-in in the preconditioner, however, memory demands may become excessive for larger or 3D grids.

The turning points and the resulting multiple stable flows are shown to be caused by a non-linear interaction between the convection term in the energy equation and the gravity term in the momentum equations. The important dimensionless parameters are Gr/Re and $Re \times Pr$. When both these parameters are sufficiently large, multiple stable flows may occur in the geometry studied. In addition, a higher Ga leads to a larger multiplicity region, although, for this phenomenon, increasing Gay–Lussac can be interpreted as effectively increasing both Gr/Re and $Re \times Pr$.

It must be stressed that geometry has an important influence on mixed convection phenomena such as

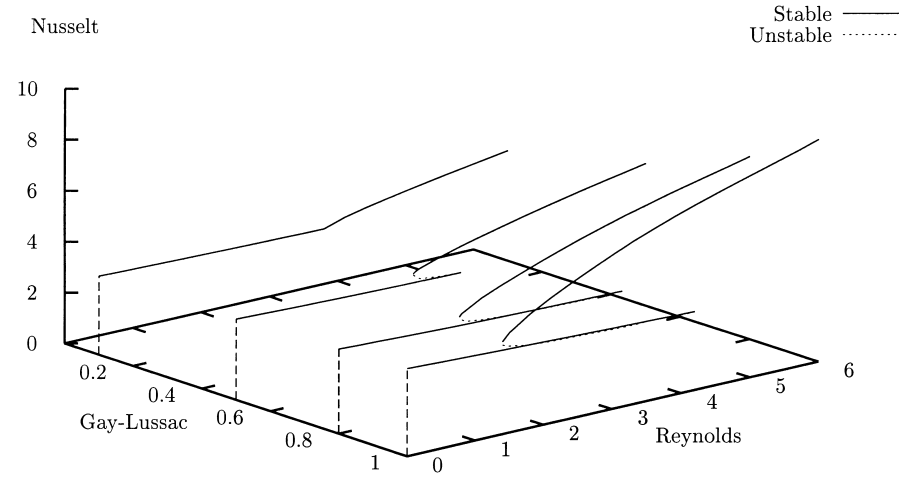

Fig. 10. Effect of Ga on the multiplicity region at $Gr = 1000$ and $Pr = 0.7$.

multiplicity. One fixed geometry has been studied in this paper, and the obtained critical values for Gr, Re, Pr (or, more accurately Gr/Re and $Re \times Pr$) and Ga are specific for this studied geometry. Relatively small alterations may suppress or favour multiplicity phenomena, or may result in different types of instabilities such as a transition to 3D and/or transient flows. For large enough values of Gr/Re and $Re \times Pr$, however, multiplicity phenomena are to be expected in other reactor geometries as well.

References

[1] Ch. Werner, J.I. Ulacia, C. Hopfmann, P. Flynn, Equipment simulation of selective tungsten deposition, J. Electrochem. Soc. 139 (2) (1992) 566–574.

[2] C.R. Kleijn, Chemical vapor deposition processes, in: M. Meyyappan (Ed.), Computational Modeling in Semiconductor Processing, Artech House, Boston, 1995, pp. 97–229 (chapter 4).

[3] C. Houtman, D.B. Graves, K.F. Jensen, CVD in stagnation point flow. An evaluation of the classical 1D treatment, J. Electrochem. Soc. 133 (5) (1986) 961–970.

[4] C.R. Kleijn, Th.H. van der Meer, C.J. Hoogendoorn, A mathematical model for LPCVD in a single wafer reactor, J. Electrochem. Soc. 136 (11) (1989) 3423–3432.

[5] K.J. Kuijlaars, C.R. Kleijn, H.E.A. van den Akker, Simulation of selective tungsten chemical vapour deposition, Solid State Electronics 42 (5) (1998) A43–A54.

[6] D.W. Hess, K.F. Jensen, T.J. Anderson, Chemical vapor deposition: a chemical engineering perspective, Reviews in Chemical Engineering 3 (2) (1985) 97–186.

[7] C.R. Kleijn, Ch. Werner, Modeling of Chemical Vapor Deposition of Tungsten Films, Birkhäuser, Basel, 1993.

[8] M. Meyyappan, Computational Modeling in Semiconductor Processing, Artech House, Boston, 1995.

[9] H. van Santen, C.R. Kleijn, H.E.A. van den Akker, Mixed convection flow instabilities in chemical vapor deposition reactors, in: Book of Late News Abstracts: 10th European Conference on CVD, Venice, Italy, 1995, p. 58.

[10] G.H. Evans, R. Greif, Effects of boundary conditions on the flow and heat transfer in a rotating disk chemical vapor deposition reactor, Numerical Heat Transfer 12 (1987) 243–252.

[11] G.H. Evans, R. Greif, A numerical model of the flow and heat transfer in a rotating disk chemical vapor deposition reactor, Journal of Heat Transfer 109 (1987) 928–935.

[12] K.F. Jensen, E.O. Einset, D.I. Fotiadis, Flow phenomena in chemical vapor deposition of thin films, Annual Reviews in Fluid Mechanics 23 (1991) 197–232.

[13] S. Joh, G.H. Evans, Heat transfer and flow stability in a rotating disk/stagnation flow chemical vapor deposition reactor, Numerical Heat Transfer A 31 (8) (1997) 867–879.

[14] A. Amahmid, M. Hasnaoui, P. Vasseur, Multiplicité des solutions en convection naturelle dans une géométrie répétitive, Int. J. Heat Mass Transfer 40 (1997) 3805–3818.

[15] D.I. Fotiadis, Two- and three-dimensional finite element simulations of reacting flows in chemical vapor deposition of compound semiconductors, Ph.D. Thesis, University of Minnesota, Minneapolis, USA, 1990.

[16] D.I. Fotiadis, S. Kieda, K.F. Jensen, Transport phenomena in vertical reactors for metalorganic vapor phase epitaxy: I. Effects of heat transfer characteristics, reactor geometry, and operating conditions, J. Crystal Growth 102 (1990) 441–470.

[17] K.F. Jensen, D.I. Fotiadis, T.J. Mountziaris, Detailed models of the MOVPE process, J. Crystal Growth 107 (1991) 1–11.

[18] C.R. Kleijn, Transport phenomena in chemical vapor deposition reactors, Ph.D. Thesis, Delft University of Technology, 1991.

[19] H.B. Keller, Numerical solution of bifurcation and nonlinear eigenvalue problems, in: P.H. Rabinowitz (Ed.), Applications of Bifurcation Theory, Marcel Dekker, New York, 1977, pp. 45–52.

[20] Y. Yamaguchi, C.J. Chang, R.A. Brown, Multiple buoyancy-driven flows in a vertical cylinder heated from below, Phil. Trans. R. Soc. Lond. A 312 (1984) 519–552.

[21] H. Van Santen, Mixed-convection instabilities in chemical vapor deposition reactors, Ph.D. thesis, Delft University of Technology, Delft, The Netherlands, 1999 (copies can be requested from the corresponding author).

[22] R.B. Bird, W.E. Stewart, E.N. Lightfood, Transport Phenomena, Wiley, New York, USA, 1960.

[23] E.P. Visser, C.R. Kleijn, C.A.M. Govers, C.J. Hoogendoorn, L.J. Giling, Return flows in horizontal MOCVD reactors studied with the use of TiO particle injection and numerical calculations, J. Crystal Growth 94 (1989) 929–946. Err 96, 732–735.

[24] J. van Kan, A second order accurate pressure-correction scheme for viscous incompressible flow, SIAM J. Sci. Stat. Comput. 7 (3) (1986) 870–891.

[25] S.V. Patankar, Numerical Heat Transfer and Fluid Flow, Hemisphere, Washington, DC, 1980.

[26] P. Wesseling, An Introduction to Multigrid Methods, Wiley, Chichester, UK, 1992.

[27] G. Wittum, On the convergence of multi-grid method with transforming smoothers, Numer. Math. 57 (1990) 15–38.

[28] J. Ortega, W. Rheinboldt, Iterative Solution of Nonlinear Equations in Several Variables, Academic Press, New York, 1970.

[29] H. van Santen, D. Lathouwers, C.R. Kleijn, H.E.A. van den Akker, Influence of segregation on the efficiency of finite volume methods for the incompressible Navier–Stokes equations, in: Proceedings of the ASME Fluids Engineering Division Summer Meeting — 1996. FED, Vol. 238, 1996, pp. 151–157.

[30] W.H. Press, S.A. Teukolski, W.T. Vetterling, B.P. Flannery, Numerical Recipes, Cambridge University Press, New York, 1988.

[31] Y. Saad, M.H. Schultz, GMRES: a generalized minimum residual algorithm for solving non-symmetric lin-

ear systems, SIAM J. Sci. Stat. Comput. 7 (1986) 869–931.
[32] R. Barrett, M. Berry, T. Chan, J. Demmel, J. Donato, J. Dongarra, V. Eijkhout, R. Pozo, C. Romine, H. van der Vorst, Templates for the Solution of Linear Systems: Building Blocks for Iterative Methods, SIAM, Philadelphia, 1992 (can be obtained through anonymous ftp at netlib2.cs.utk.edu in the directory/templates).
[33] W. Hackbusch, Iterative Solution of Large Sparse Systems Equations, Springer, New York, 1994.
[34] Y. Saad, Iterative Methods for Sparse Linear Systems, PWS, Boston, 1996.
[35] J.A. Meijerink, H.A. van der Vorst, Guidelines for the usage of incomplete decompositions in solving sets of linear equations as they occur in practical problems, J. Comput. Physics 44 (1981) 134–155.
[36] H.A. van der Vorst, High performance preconditioning, SIAM J. Sci. Stat. Comput. 10 (2) (1989) 1174–1185.
[37] C. Vuik, A. Segal, Solution of the coupled Navier–Stokes equations, in: W. Hackbusch, G. Wittum (Eds.) Numerical treatment of coupled systems, Proceedings of the Eleventh GAMM-Seminar, Kiel, 1995, pp. 186–197, Technical Report 95–28 (can be obtained through anonymous ftp at ftp://ftp.twi.tudelft.nl in directory/pub/publications/tech-reports/1995).
[38] A. van der Ploeg, Preconditioning for sparse matrices with applications, Ph.D. Thesis, Rijksuniversiteit Groningen, The Netherlands, 1994.